

Coupled-mode-induced transparency and attenuation resulting from cross-polarization couplingKhoa V. Bui^{1,2} and A. T. Rosenberger^{1,*}¹*Department of Physics, Oklahoma State University, Stillwater, Oklahoma 74078, USA*²*School of Engineering Physics, Hanoi University of Science and Technology, Hanoi 100000, Vietnam*

(Received 31 December 2019; accepted 2 March 2020; published 23 March 2020)

Induced transparency and attenuation effects are observed in the throughput of a single whispering-gallery microresonator due to mode coupling between two coresonant orthogonally polarized whispering-gallery modes of very different quality factors. Intracavity cross-polarization coupling, occurring when either the transverse electric (TE) mode or the transverse magnetic (TM) mode is driven, results in coupled-mode induced transparency or coupled-mode induced attenuation. Coresonance between the TE and TM modes is obtained by strain tuning, and the cross-polarization coupling is produced by polarization rotation due to optical spin-orbit interaction in a slightly asymmetric resonator. The observed behavior enables slow light and fast light, i.e., the delay or advancement of an incident resonant pulse. Experimental results representative of several different types of behavior are presented here. Induced transparency is seen to be accompanied by pulse delay, whereas induced attenuation can involve pulse advancement or delay. The results are analyzed and explained by analytical modeling and by comparison to the output of a more detailed numerical model describing these effects. Delays of up to 170 ns and advancements of up to 14 ns are found. The observed range of cross-polarization coupling strengths (probability of polarization change per round trip), namely, 10^{-10} – 10^{-7} , is in agreement with theory.

DOI: [10.1103/PhysRevA.101.033836](https://doi.org/10.1103/PhysRevA.101.033836)**I. INTRODUCTION**

Induced transparency with pulse delay and induced attenuation with pulse advancement in optical microresonator systems have the potential to be exploited for various applications, as in signal processing and several types of optical sensing [1–16]. In addition, the importance of polarization effects in whispering-gallery microresonators is increasingly becoming recognized and studied [17–22]. The work reported in this paper involves induced transparency and attenuation resulting from the coupling of orthogonally polarized modes in a microresonator [22].

The throughput of a single microresonator can exhibit induced transparency or induced attenuation effects. In this work, these are observed when tunable laser light is injected via a tapered-fiber coupler into a fused-silica whispering-gallery resonator that has two coresonant (frequency-degenerate) whispering-gallery modes (WGMs) having very different quality factors (Q s). Induced transparency is generally accompanied by pulse delay (slow light), whereas induced attenuation can show pulse delay or pulse advancement (fast light). Coresonance can be introduced in a controllable way by strain tuning. The resonator has two orthogonally polarized families of modes, TE (transverse electric) and TM (transverse magnetic). Because the birefringence induced by strain tuning causes the two families of modes to tune at different rates, it can be used to impose frequency degeneracy between a TE mode and a TM mode.

The method for achieving induced transparency and attenuation uses cross-polarization coupling (CPC). The light of

one polarization circulating in a WGM of the microresonator can be coupled into a coresonant WGM of the orthogonal polarization. This CPC is a result of weak polarization rotation [22]. The input light and detected throughput are of one polarization, say TE. Because of CPC, the interaction with a coresonant TM WGM produces a throughput spectrum (as the driving laser is scanned in frequency) showing cross-polarization coupled-mode-induced transparency, or attenuation (CMIT, CMIA). An input pulse whose center frequency is resonant will be delayed or advanced. These effects are similar to the coupled-resonator-induced transparency and attenuation observed in coupled whispering-gallery microresonators [4,10,23–28], except that output from the nondriven WGM can also be detected here.

A simple model has been used to study the effects observed and to fit experimental results. In this fitting procedure, there are three adjustable parameters: the CPC strength is a nearly free parameter, having only weak constraints set by other experimental observations; the slight offsets of one WGM's frequency from the other and from the pulse center frequency are semifree parameters, being rather tightly constrained by observation of the throughput dips of the two WGMs. The fittings determine the CPC strengths to be in agreement with theory and allow comparison of experimental and model pulse delay and advancement times.

Using a single resonator is a significant simplification over coupled-resonator systems. Other observations of CMIT in a single resonator have been reported [2–4,29–36], but nearly all of them involve the coupling of WGMs of the same polarization but different radial orders, and pulse delay and advancement have not been reported in comparable detail [28,37]. The use of linear cross-polarization coupling between whispering-gallery modes, whose strength can be calculated if

*atr@okstate.edu

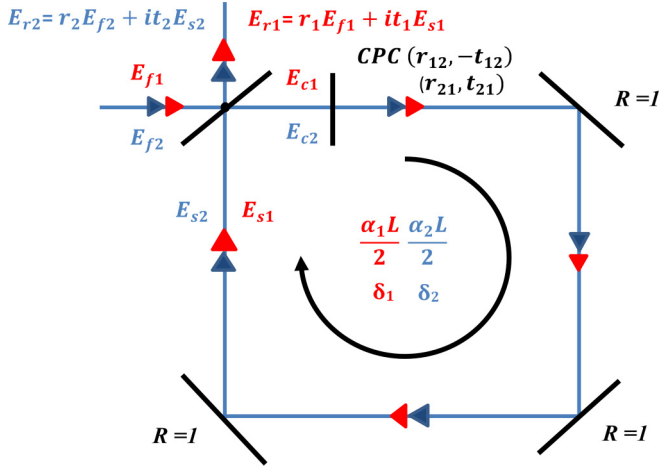


FIG. 1. Ring cavity representing tapered-fiber coupling to a microresonator with intracavity cross-polarization coupling.

the orders of the coupled WGMs are known [22], makes this work unique, and observation of the orthogonal throughput confirms that CPC is responsible for the mode coupling. The previously reported WGM cross-polarization coupling was nonlinear [35], and coupling among three modes of different polarizations has been reported in a microfiber knot resonator [36]. Our pulse delays, while greater than most reported earlier [28,37], are comparable to those achievable with a single WGM. The advantage of CMIT is that the amplitude of the throughput pulse, located at the IT peak, can be significantly larger than that in the single-WGM case, where the delayed pulse is at the bottom of a very deep throughput dip and is therefore attenuated.

The rest of the paper is structured as follows. The next section develops the model, both steady state and time dependent. The third section describes the experimental setup and procedure, the fourth section presents results and discussion, and the last section concludes this work.

II. MODEL

We begin with a steady-state model based on a simple ring cavity with one partially transmitting mirror. This is sketched in Fig. 1.

In Fig. 1, the subscripts 1 and 2 refer to the two orthogonal polarizations. E_{fj} is the input amplitude of polarization j , and

$$E_{rj} = r_j E_{fj} + i t_j E_{sj} \quad (1)$$

is the throughput amplitude of polarization j . E_{sj} is the intracavity mode amplitude just before output coupling, and the input-output coupling coefficient is $i t_j$, with $r_j^2 = 1 - t_j^2 = 1 - T_j$. Although the input and output coupling coefficients are different in general [38], for our conditions that difference is only about 5%, so they are taken to be equal [39]. The intracavity mode amplitudes just after input coupling are

$$E_{cj} = i t_j E_{fj} + r_j E_{sj}, \quad (2)$$

and the various intracavity amplitudes are related by

$$\begin{aligned} E_{s1} &= (r_{12} E_{c1} - t_{12} E_{c2}) \exp\left(-\frac{1}{2} \alpha_1 L + i \delta_1\right) \\ E_{s2} &= (r_{21} E_{c2} + t_{21} E_{c1}) \exp\left(-\frac{1}{2} \alpha_2 L + i \delta_2\right). \end{aligned} \quad (3)$$

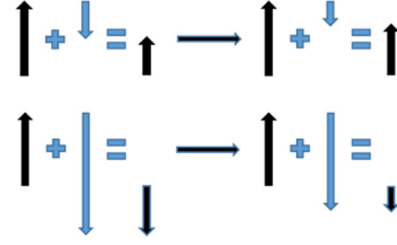


FIG. 2. Origin of induced effects. Uncoupled field plus outcoupled field gives net throughput field; CPC reduces the outcoupled field, as seen on the right. Top: undercoupled mode 1 leads to CMIT. Bottom: overcoupled mode 1 leads to CMIA.

In Eqs. (3), δ_j and $\alpha_j L$ are the round-trip phase (modulo 2π) and intrinsic loss for mode j ; L is the resonator circumference. Cross-polarization coupling is represented in Fig. 1 as an effective intracavity wave plate and expressed by the coefficients t_{12} and t_{21} , where $t_{12}^2 = 1 - r_{12}^2$ and $t_{21}^2 = 1 - r_{21}^2$ are the polarization rotation probabilities per round trip, called T_s and T_p in Ref. [22].

It can now be seen qualitatively how the interference between the driven low- Q mode 1 and the coresonant high- Q mode 2 produces CMIT and CMIA. The intracavity field E_{s1} is excited directly by input coupling and indirectly by cross-polarization coupling into E_{s2} and back into E_{s1} . The indirect path involves a factor of $-T_c$, where

$$T_c = t_{12} t_{21}. \quad (4)$$

The destructive interference due to CPC thus reduces the intracavity amplitude E_{s1} . The fraction of this that couples out is out of phase with the uncoupled part of the throughput because of the product of input and output coupling coefficients. The simplest possible case is described here. If mode 1 is undercoupled, as in the top part of Fig. 2, the net throughput for mode 1 alone, shown on the left, is reduced from the input to produce the usual resonance dip; but near resonance, as on the right, where mode 2 is also excited, the reduced mode 1 intracavity amplitude results in greater throughput, identified as induced transparency. For mode 1 overcoupled, as in the bottom part of Fig. 2, the outcoupled amplitude is greater than the uncoupled amplitude, and the effect of mode 2 on resonance is to reduce the throughput and produce induced attenuation.

Equations (1)–(3) constitute the steady-state model; from the recognition that the terms on the right sides of Eqs. (3) are actually one round trip earlier than the terms on the left, time evolution equations can be derived for the intracavity amplitudes:

$$\begin{aligned} \frac{d}{dt} E_{s1} &= -\gamma_1 E_{s1} - \frac{t_{12}}{\tau_{r1}} E_{s2} + \frac{i t_1}{\tau_{r1}} E_{f1} - \frac{i t_2 t_{12}}{\tau_{r1}} E_{f2}, \\ \frac{d}{dt} E_{s2} &= -\gamma_2 E_{s2} + \frac{t_{21}}{\tau_{r2}} E_{s1} + \frac{i t_2}{\tau_{r2}} E_{f2} + \frac{i t_1 t_{21}}{\tau_{r2}} E_{f1}. \end{aligned} \quad (5)$$

With these and Eq. (1), the time evolution of the throughput amplitudes can be found. In Eqs. (5), $\tau_{rj} = n_j L / c$ is the round-trip time for mode j , where n_j is the effective refractive

index of the mode, and

$$\gamma_j = \frac{T_j + \alpha_j L}{2\tau_{rtj}} - i \frac{\delta_j}{\tau_{rtj}} = \kappa_j(1 + i\theta_j), \quad (6)$$

with κ_j being the amplitude decay rate, or half the inverse of the photon lifetime in mode j , and θ_j being the offset of the resonant frequency of mode j from the input frequency in units of half the mode linewidth.

A numerical solution of the steady-state and time-dependent models is done using input in terms of experimentally measurable quantities. These quantities include the resonator diameter, the quality factors of the modes, their resonant dip depths and coupling regimes, the detuning of mode 2's resonant frequency from that of mode 1 (if any), and, for the pulse response, the input pulse width and its center frequency detuning from mode-1 resonance. The CPC strength $T_c = t_{12}t_{21}$ is input as a free fitting parameter for comparing steady-state model output to experimental throughput spectra; although t_{12} and t_{21} are input separately, the mode-1 throughput depends only on their product. In addition, the two detunings are not known with perfect precision and are treated as semifree parameters.

Knowledge of the input frequency ν and measurement of the mode linewidth (FWHM of a throughput dip) $\Delta\nu_j$ gives the quality factor Q_j of mode j and its total loss $T_j + \alpha_j L$:

$$Q_j = \frac{\nu}{\Delta\nu_j} = \frac{2\pi n_j L}{\lambda(T_j + \alpha_j L)}, \quad (7)$$

where λ is the vacuum wavelength. The coupling and intrinsic losses can be determined individually from the fractional dip depth M_j and the coupling regime:

$$M_j = \frac{4x_j}{(1+x_j)^2}, \quad \text{where } x_j = \frac{T_j}{\alpha_j L}. \quad (8)$$

Undercoupling and overcoupling mean $x_j < 1$ and > 1 , respectively; a given M_j can occur for two values of x_j whose product is 1, so knowledge of the coupling regime determines the values of T_j and $\alpha_j L$. The one remaining parameter in the model consisting of Eqs. (1)–(5) is the round-trip phase δ_j , which is related to the detuning of the input light frequency ν from the mode j resonance frequency ν_j by

$$\delta_j = \frac{2\pi n_j L}{c}(\nu - \nu_j). \quad (9)$$

In this work, only polarization 1 is input ($E_{f2} = 0$), and the CMIT effects are observed in the mode-1 throughput.

A numerically modeled example of CMIT response is given in the next three figures, in which the wavelength input to mode 1 is taken to be 1550 nm, the microresonator radius is 300 μm ($L = 1.88$ mm), $Q_1 = 5 \times 10^6$, $Q_2 = 1 \times 10^8$, $M_1 = 0.8$, $M_2 = 0.7$, $T_c = 5 \times 10^{-8}$, both modes are undercoupled, and the detuning of mode 2 from mode 1 is zero. Figure 3 shows the throughput spectrum calculated from Eqs. (1)–(3), that is, $|E_{r1}/E_{f1}|^2$ as a function of the input frequency relative to the modes' resonant frequency. In Fig. 3, the enhanced throughput on resonance is due to IT, interference between the two modes of very different Q values. There is no true mode splitting, because T_c is lower than the critical, or exceptional-point, value, above which the supermode frequencies split and ATS (Autler-Townes splitting) occurs [40]. This critical value

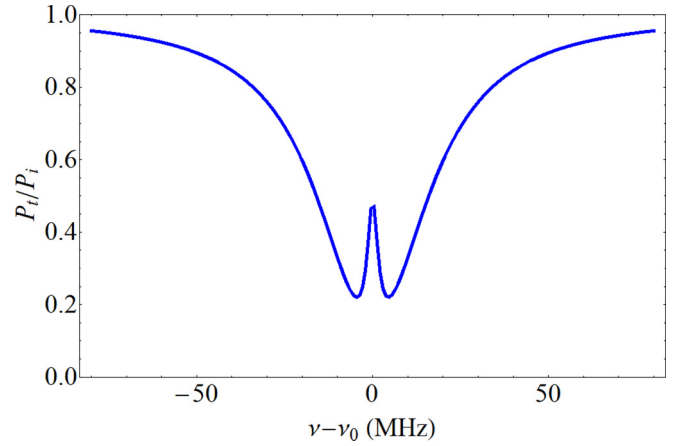


FIG. 3. Modeled CMIT throughput spectrum: $Q_1 = 5 \times 10^6$, $Q_2 = 1 \times 10^8$, $M_1 = 0.8$, $M_2 = 0.7$, $T_c = 5 \times 10^{-8}$, both modes undercoupled, mode 2 coresonant with mode 1.

can be found by taking the second time derivative of the first of Eqs. (5) in the case of resonance and zero input to find

$$\ddot{E}_{s1} + (\kappa_1 + \kappa_2)\dot{E}_{s1} + \left(\kappa_1\kappa_2 + \frac{T_c}{\tau_{rt1}\tau_{rt2}}\right)E_{s1} = 0. \quad (10)$$

Then substituting $E_{s1} \propto \exp(\lambda t)$ results in

$$\lambda = -\frac{\kappa_1 + \kappa_2}{2} \pm \sqrt{\left(\frac{\kappa_1 - \kappa_2}{2}\right)^2 - \frac{T_c}{\tau_{rt1}\tau_{rt2}}}, \quad (11)$$

showing the onset of ATS when T_c is large enough to make the radicand negative and produce frequency splitting.

The model also calculates the phase ϕ of E_{r1} relative to E_{f1} , and this is plotted vs input frequency in Fig. 4. The positive slope on resonance (positive dispersion) indicates that a group delay will be experienced by an input pulse. The group delay is given by

$$\tau_d = \frac{1}{2\pi} \frac{d\phi}{d\nu}. \quad (12)$$

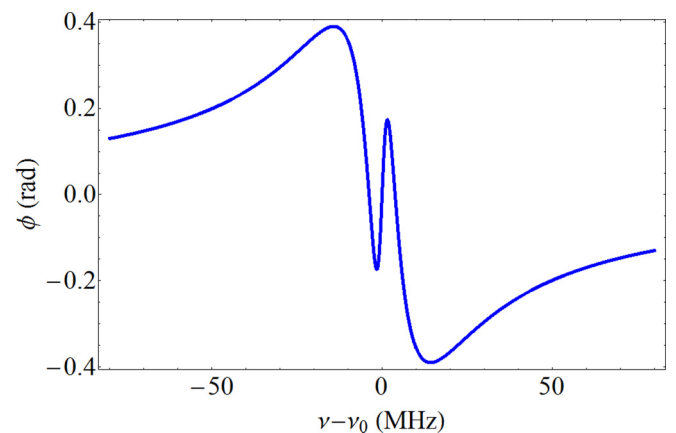


FIG. 4. Modeled CMIT throughput phase relative to input for the same parameter values as in Fig. 3.

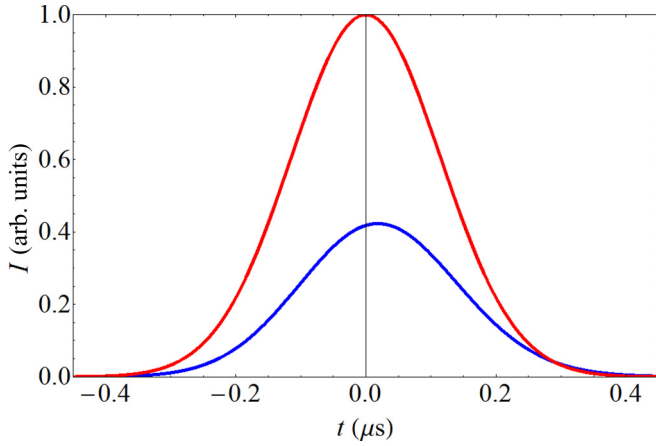


FIG. 5. Modeled CMIT pulse delay for the same parameter values as in Fig. 3. The upper red curve is the input reference pulse; the lower blue curve is the delayed throughput pulse.

The range of frequencies over which the positive slope occurs near resonance is approximately the same as the linewidth of mode 2. In the model, a Gaussian pulse $E_{f1}(t)$ having a width of 230 ns is input. This pulse width corresponds to a pulse bandwidth equal to, or slightly less than, the linewidth of mode 2. The center frequency of this pulse has a zero detuning from resonance, and Fig. 5 shows how the throughput pulse on resonance, calculated from Eqs. (5) plus the time derivative of Eq. (1) (with $E_{f2} = 0$, $\delta_1 = 0$, and $\delta_2 = 0$), is delayed with respect to the input pulse. The peak intensity of the input pulse is set to be 1, and the delayed pulse is scaled accordingly.

Modeled CMIA response is shown in the next three figures; again, the wavelength is 1550 nm and the microresonator radius is 300 μm . Now $Q_1 = 5 \times 10^6$, $Q_2 = 1 \times 10^8$, $M_1 = 0.5$, $M_2 = 0.9$, $T_c = 1.6 \times 10^{-8}$, both modes are overcoupled, the pulse width is 230 ns, and the detuning and pulse detuning are both zero. Figure 6 shows the throughput spectrum, Fig. 7 shows the phase ϕ of E_{r1} relative to E_{f1} plotted vs input

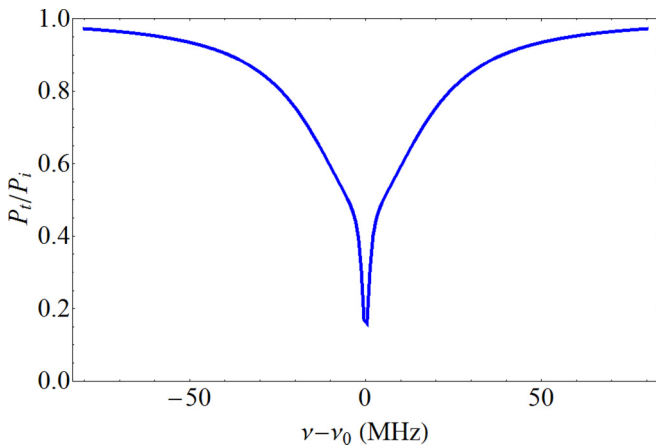


FIG. 6. Modeled CMIA throughput spectrum: $Q_1 = 5 \times 10^6$, $Q_2 = 1 \times 10^8$, $M_1 = 0.5$, $M_2 = 0.9$, $T_c = 1.6 \times 10^{-8}$, both modes overcoupled, mode 2 coresonant with mode 1.

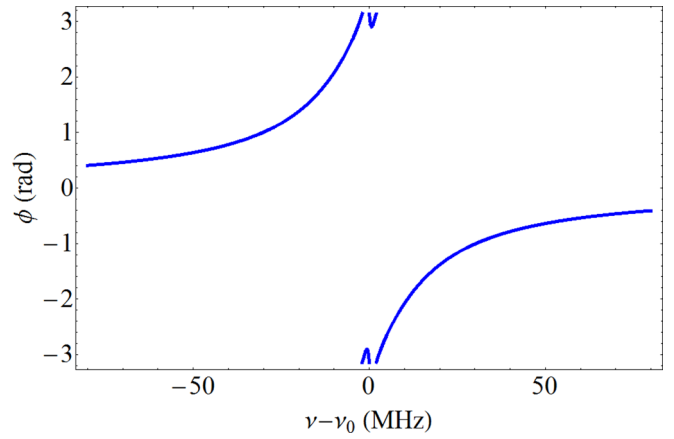


FIG. 7. Modeled CMIA throughput phase relative to input for the same parameter values as in Fig. 6.

frequency, and Fig. 8 shows pulse advancement resulting from the negative dispersion on resonance seen in Fig. 7.

It is also possible to have pulse delay under CMIA conditions; in fact, if the CPC strength is reduced by about 20%, with the other parameters unchanged from Figs. 6–8, the pulse advancement seen in Fig. 8 becomes a delay comparable to that of Fig. 5.

III. EXPERIMENTAL SETUP AND PROCEDURE

The experimental setup is shown in Fig. 9. A description of its components follows.

The light source is a tunable diode laser (New Focus, model 6328) operating in the spectral range from 1508 to 1580 nm and scanned in frequency by function generator FG1 (Wavetek, model 395). The free-space beam passes through an anamorphic prism (AP) and an optical isolator (OI) before entering an acousto-optic modulator (AOM) (Isomet, model 1250C, 235A-1 driver), which can be controlled by waveform generator FG2 (Wavetek, model 395), to produce cw transmission or Gaussian pulses. After passing through a set of wave plates (WP) to control the input polarization, the

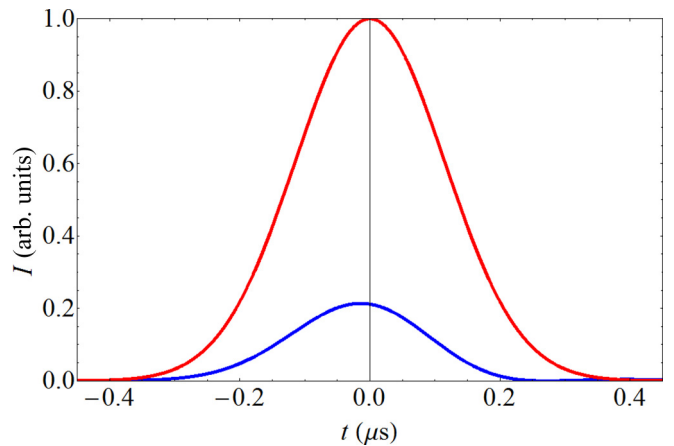


FIG. 8. Modeled CMIA pulse advancement for the same parameter values as in Fig. 6. The upper red curve is the input reference pulse; the lower blue curve is the advanced throughput pulse.

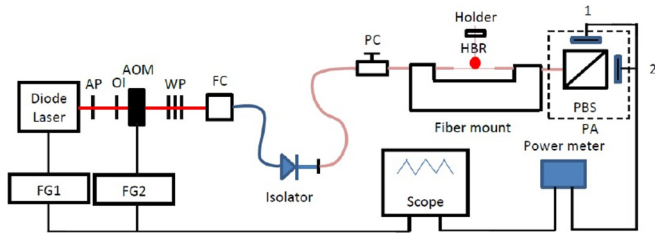


FIG. 9. Experimental setup.

free-space beam is injected using a fiber coupler (FC) into a fiber isolator that prevents any backward-propagating light from reflecting from the fiber input face and giving rise to Fabry-Pérot fringes in the throughput. The fiber isolator connects to a single-mode fiber that passes through a compression-based polarization controller (PC) for further regulation of the input light. This fiber is adiabatically bitapered and brought into contact with the microresonator in its equatorial plane using a three-dimensional (3D) translation stage. Outcoupled light is collimated and sent to a polarization analyzer (PA) which includes a polarizing beam splitter (PBS) and two detectors, one slow (Newport, model 818-IR) and one fast (Thorlabs, model SIR5-FC). The entire polarization analyzer can be rotated about the incoming fiber axis to change the detection basis. The detector outputs are sent to a power meter (Newport, model 2832-C) or directly to the oscilloscope, which is further connected to a laptop computer (not shown) for additional data analysis.

The laser frequency-scan rate is carefully calibrated so that an accurate value of Q can be determined by measuring the width of a throughput dip. The microresonator, a hollow bottle resonator (HBR) [41,42] consisting of a thin-walled silica capillary with a bulged region created by heating and pressurizing, is mounted in an acrylic box to minimize temperature fluctuations and other effects of air currents. Details of the fabrication and characterization of the HBR can be found in Refs. [43,44]. It is mounted with its axis vertical (out of the page in Fig. 9) so that its TE modes have vertical polarization and would be detected by detector 1 in the analyzer orientation shown, and its TM modes have horizontal polarization detected by detector 2. The HBR is held by an apparatus that allows piezoelectrically controlled strain tuning by axial stretching. Because modes of orthogonal polarizations strain-tune at different rates [45–47], this allows co-resonance between a TE mode and a TM mode to be achieved as desired. This is similar to other strain-tuning methods that tune WGMs of the same polarization but different radial orders at different rates [31,48].

The waist of the tapered coupling fiber has a radius of approximately $1 \mu\text{m}$ and supports many different modes. Despite this, it acts as a single-mode fiber because the taper transitions are adiabatic and only its fundamental mode has appreciable coupling to the WGMs of the HBR [39]. It is normally positioned in contact at the equator (maximum radius) of the HBR but can be moved away from the equator to excite a different set of WGMs; this does not affect the measurements reported here. The length of the coupling fiber from the polarization controller to the polarization analyzer is kept straight to minimize any effect on the polarization. That

the fiber does not affect the polarization after coupling to the HBR is confirmed experimentally by the following method. With the analyzer rotated 45° from its position in Fig. 9 (0°), each detector shows throughput dips for WGMs of both polarizations. The input polarization is then adjusted until about half the dips disappear; this means that the polarization incident on the HBR is pure linear TE or TM, and upon rotation of the analyzer back to 0° , the signal on one detector is zero. This observation, when mode 2 is not co-resonant with mode 1, confirms that the input polarization driving mode 1 is an eigenpolarization (TE or TM) of the resonator basis. Therefore, as we discussed previously [22], there is no possibility of polarization conversion independent of CPC. Likewise, input linearly polarized at 45° polarization can be verified by rotating the analyzer to 45° and adjusting the polarization control until there is no signal on the orthogonal detector. Finally, with the input polarization and the analyzer both at 0° , the $|E_{r2}|^2$ signal observed on the orthogonal detector vanishes when mode 2 is taken out of co-resonance with mode 1. Thus we are confident that the main signal accurately represents $|E_{r1}|^2$.

The experimental procedure for investigating CMIT or CMIA is as follows. With the input polarization linear and aligned with the HBR basis, so that only TE or TM modes are being excited, a low- Q mode is found. The HBR is then strain tuned; if a CMIT/CMIA feature appears, along with output on the orthogonal polarization to confirm that the two interacting WGMs have orthogonal polarizations, the modes are tuned away from co-resonance and individually characterized. The tuning is done after changing the input polarization to 45° so that with the analyzer at 0° , the interacting modes can be seen on different detectors. Then the input is changed to TE to determine the Q , dip depth M , and coupling regime of that mode, followed by a change to TM to characterize the other mode. The coupling regime is determined by augmenting the intrinsic loss through touching the opposite side of the HBR with a tapered-fiber end; the dip depth will increase if the mode is overcoupled and will decrease if the mode is undercoupled. The CMIT/CMIA feature is then recovered

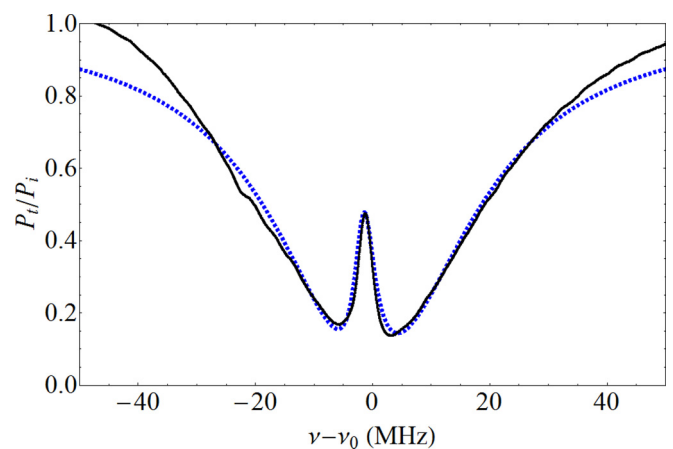


FIG. 10. CMIT with $172\text{-}\mu\text{m}$ -radius HBR. Experimental (solid black line) and model (dashed blue line) throughput spectra. Parameter values: $T_c = 2.24 \times 10^{-8}$, detuning = -1.5 MHz , $M_1 = 0.87$ (undercoupled), $M_2 = 0.30$ (undercoupled), $Q_1 = 4.75 \times 10^6$, $Q_2 = 1.0 \times 10^8$.

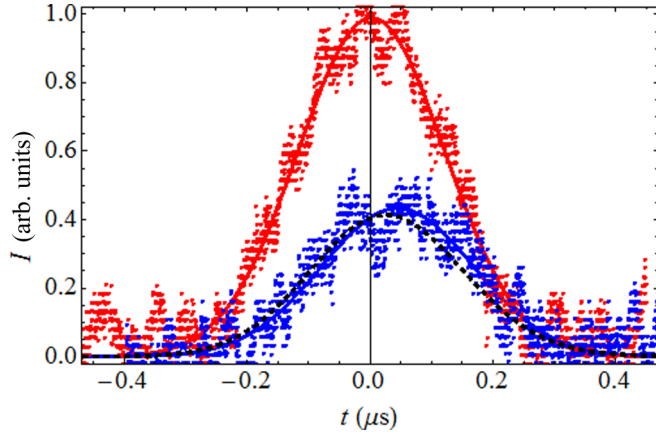


FIG. 11. Pulse delay in CMIT. Parameters as in Fig. 10, with pulse detuning of -1.5 MHz. Experimental input (upper, noisy trace and solid red line) and throughput (lower, noisy trace and solid blue line) pulses, with an input pulse width of 275 ns and a delay of 42 ns, and model throughput pulse (dashed black line), with a delay of 27 ns.

and the throughput spectrum is recorded. The AOM is then set to produce a train of Gaussian pulses of nominal width 270 ns and period 1140 ns, with the laser still being scanned in frequency. A resonant throughput pulse is recorded and compared to an off-resonance pulse displaced by an integer number of pulse periods to find the delay or advancement of the resonant pulse. (Off resonance, where no coupling into the microresonator takes place, the throughput pulse should be the same as the input pulse.) The throughput spectrum is then fit to the model as described above to determine the value of T_c , and using that value of T_c , the model pulse is compared to the experimental pulse.

IV. RESULTS AND DISCUSSION

Four results are shown in Figs. 10–17. These are examples of the various cases observed: CMIT with pulse delay

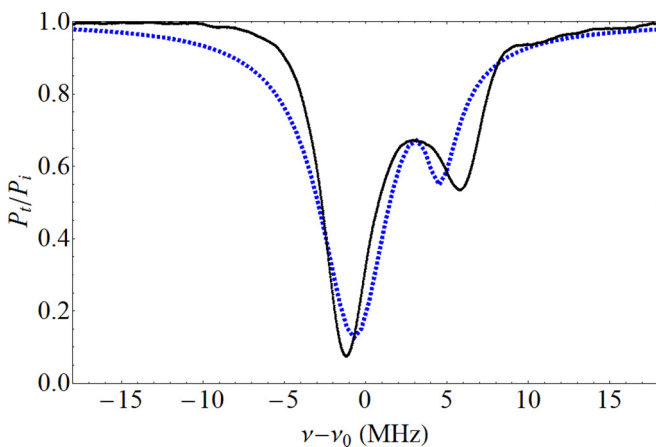


FIG. 12. ATS with 170- μm -radius HBR. Experimental (solid black line) and model (dashed blue line) throughput spectra. Parameter values: $T_c = 3.55 \times 10^{-9}$, detuning = 3.8 MHz, $M_1 = 0.896$ (undercoupled), $M_2 = 0.62$ (undercoupled), $Q_1 = 3.5 \times 10^7$, $Q_2 = 1.0 \times 10^8$.

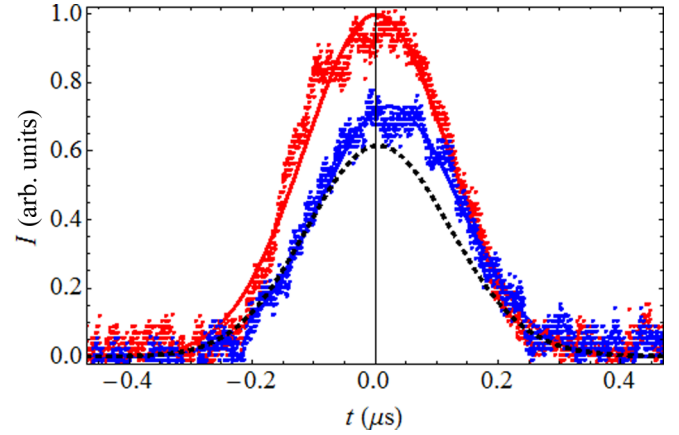


FIG. 13. Pulse delay in ATS. Parameters as in Fig. 12, with pulse detuning of 3.4 MHz. Experimental input (upper, noisy trace and solid red line) and throughput (lower, noisy trace and solid blue line) pulses, with an input pulse width of 270 ns and a delay of 22 ns, and model throughput pulse (dashed black line), with a delay of 9 ns.

(Figs. 10 and 11), ATS with pulse delay (Figs. 12 and 13), CMIA with pulse advancement (Figs. 14 and 15); and CMIA with pulse delay (Figs. 16 and 17). The first of each pair of figures shows the experimental throughput spectrum along with the model spectrum in which T_c has been adjusted to give the best fit. In each case, the estimated experimental detuning of mode 2 from mode 1 has been incorporated in the model, along with the measured dip depths, coupling regimes, and quality factors. The second figure in each pair displays the effective input (off-resonance) pulse together with the delayed or advanced resonant throughput pulse, each noisy experimental trace having been fitted to a Gaussian; the model throughput pulse, at the estimated experimental pulse center frequency detuning, is also shown. All pulse heights are relative to that of the fitted experimental input pulse.

In Figs. 10–17, the uncertainty in measuring the dip depths M_j is about $\pm 2\%$, and the quality factors Q_j are measured

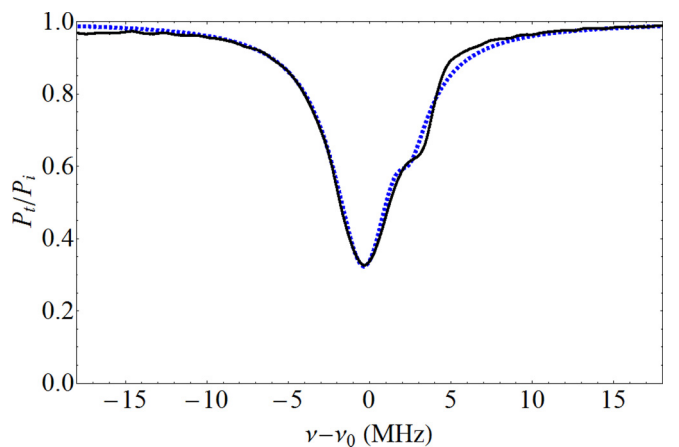


FIG. 14. CMIA with 170- μm -radius HBR. Experimental (solid black line) and model (dashed blue line) throughput spectra. Parameter values: $T_c = 7.94 \times 10^{-10}$, detuning = 2.0 MHz, $M_1 = 0.70$ (undercoupled), $M_2 = 0.68$ (overcoupled), $Q_1 = 4.0 \times 10^7$, $Q_2 = 1.0 \times 10^8$.

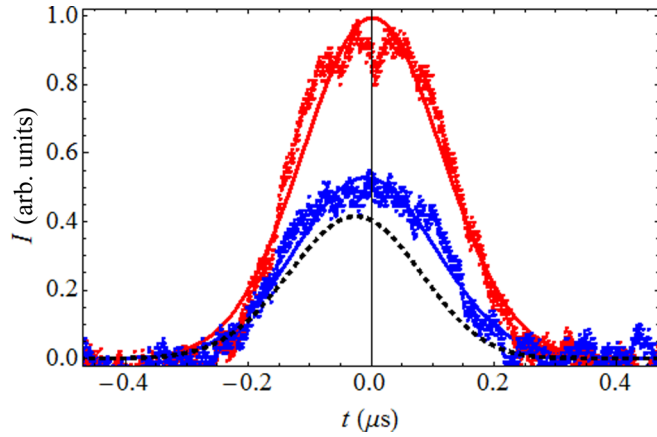


FIG. 15. Pulse advancement in CMIA. Parameters as in Fig. 14, with pulse detuning of -0.8 MHz. Experimental input (upper, noisy trace and solid red line) and throughput (lower, noisy trace and solid blue line) pulses, with an input pulse width of 265 ns and an advancement of 14 ns, and model throughput pulse (dashed black line), with an advancement of 25 ns.

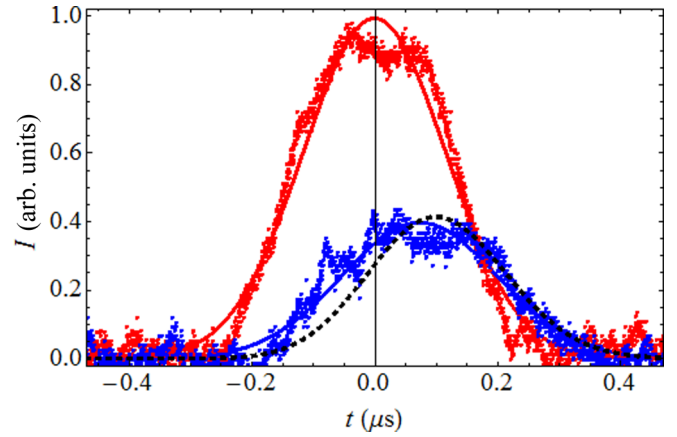


FIG. 17. Pulse delay in CMIA. Parameters as in Fig. 16, with pulse detuning of 0.3 MHz. Experimental input (upper, noisy trace and solid red line) and throughput (lower, noisy trace and solid blue line) pulses, with an input pulse width of 265 ns and a delay of 75 ns, and model throughput pulse (dashed black line), with a delay of 97 ns.

to within about $\pm 5\%$. These uncertainties have little effect on determining the CPC strength; its uncertainty in fitting by eye is about $\pm 20\%$. The detuning is known to ± 0.1 MHz and the pulse detuning to ± 0.2 MHz. The experimental pulse delay or advancement is uncertain by ± 10 ns, and the model delay or advancement is uncertain by ± 5 ns. The experimental delay uncertainty is larger because noise on the relatively weak signal from the fast detector makes the Gaussian fitting somewhat imprecise.

The results from Figs. 10–17, along with a few additional cases, are summarized in Table I; the first four entries correspond to the four pairs of figures. From Table I, the range of values of T_c is seen to correspond to the range (10^{-10} – 10^{-7}) predicted by theory [22]. The sign of the delay is consistent between experiment and model, but not every case agrees quantitatively. There are two potential explanations for this.

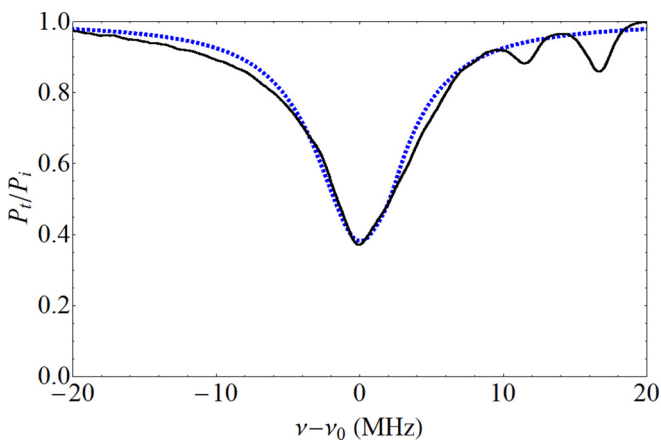


FIG. 16. CMIA with 172- μm -radius HBR. Experimental (solid black line) and model (dashed blue line) throughput spectra. Parameter values: $T_c = 7.94 \times 10^{-11}$, detuning = 2.0 MHz, $M_1 = 0.61$ (overcoupled), $M_2 = 0.83$ (overcoupled), $Q_1 = 2.6 \times 10^7$, $Q_2 = 1.0 \times 10^8$.

One experimental complication that is not accounted for in the model is mode overlap. For example, additional modes of the same polarization as mode 1 are noticeable in Fig. 16. It is also possible that other modes are near enough to overlap with mode 1 and affect the throughput spectral profile. In addition, there may be nearby modes of the orthogonal polarization that modify the throughput profile. All mode overlap was avoided as much as possible, but it is always a potential source of discrepancy between experiment and model, affecting both the CPC strength determination and delay agreement. For example, if the reference pulse is off resonance with mode 1 but near resonance with another mode, the reference (input) pulse will be smaller in height and perhaps delayed or advanced itself. This may be why the experimental resonant pulse is taller than the model pulse in Figs. 13 and 15. The other possible explanation for experiment-model disagreement is that the model pulse delay is rather sensitive to the assumed value of the pulse center frequency detuning. Its uncertainty is about 0.2 MHz, but a pulse detuning error of up to 2–3 times that would be enough to produce agreement with experimental pulse delay in most cases.

TABLE I. Summary of results for CPC strength and pulse delay (negative delay indicates advancement).

Effect	Q_1, Q_2 ($\times 10^7$)	T_c ($\pm 20\%$) ($\times 10^{-8}$)	Expt. Delay (ns ± 10)	Model Delay (ns ± 5)
CMIT	0.475, 10	2.24	42	27
ATS	3.5, 10	0.355	22	9
CMIA	4.0, 10	0.079	-14	-25
CMIA	2.6, 10	0.008	75	97
CMIT	1.1, 9.5	1.51	50	25
CMIA	2.9, 9.3	0.0398	-13	-17
CMIA	3.5, 10	0.010	170	125

V. CONCLUSIONS

Coupled-mode induced transparency and attenuation (CMIT, CMIA) have been modeled and observed in detail in a tapered-fiber-coupled hollow bottle resonator. The process responsible for the coupling between whispering-gallery modes (WGMs) has been confirmed to be cross-polarization coupling (CPC) between one TE WGM and one TM WGM. In a previous work [22], the range of the strength of CPC was calculated from first principles, and the CPC strengths determined here by fitting experiment to model fall within that range.

The model shows that the occurrence of CMIT should be accompanied by an enhanced positive dispersion, leading to pulse delay. The observed delays are in reasonable agreement with those predicted by the model when experimental parameters are input. Likewise, CMIA can be accompanied by pulse advancement resulting from negative dispersion or by pulse delay. Again, experiment and model are in reasonable agreement. Note that the observed delays, and to a lesser degree the advancements, are a substantial fraction of the overall pulse width of about 270 ns. To emphasize the scale, 50 ns would be the delay produced by about a 10-m length of fiber.

These results show that the intracavity coupling between WGMs of orthogonal polarizations can give rise to induced phenomena that have previously been shown to have potential applications. These include signal processing and sensing enhancement. For example, in cases where the detuning between WGMs is about half the linewidth of the lower- Q mode, the

central IT spike becomes an offset Fano resonance with a steep profile that can be used for dispersive sensing.

Investigation of potentially disruptive experimental conditions using the model has shown that the results presented here, the throughput spectrum of mode 1 and the pulse delay or advancement, are not appreciably affected. In particular, if the polarization analyzer is misaligned by a few degrees, or if the input polarization is misaligned by a few degrees and/or very slightly elliptical, at the expected maximum limits of both, any effect is barely noticeable in the throughput spectrum, and the CPC strength and pulse delay are not noticeably affected. However, noticeable effects can be seen in the mode-2 throughput. Modification of the experimental setup is underway to allow us to do quantitative measurements of the mode-2 output along with the results presented here. The detectors in the polarization analyzer will be replaced with a matched pair of fast detectors more sensitive than the current one. This will reduce the noise on the measured pulse traces, and should allow us to separately determine t_{12} and t_{21} . Then, using the method of Ref. [22], knowledge of their squares, T_s and T_p , may permit identification of the mode numbers for both WGMs, leading to additional potential applications.

ACKNOWLEDGMENTS

The authors wish to thank Elijah Dale, Erik Gonzales, Deepak Ganta, Razvan-Ionut Stoian, Limu Ke, Sreekul Raj Rajagopal, and Karleyda Sandoval for their assistance in making this work possible.

-
- [1] M. R. Foreman, J. D. Swaim, and F. Vollmer, Whispering gallery mode sensors, *Adv. Opt. Photon.* **7**, 168 (2015).
 - [2] Y. F. Xiao, L. He, J. Zhu, and L. Yang, Electromagnetically induced transparency-like effect in a single polydimethylsiloxane-coated silica microtoroid, *Appl. Phys. Lett.* **94**, 231115 (2009).
 - [3] B. B. Li, Y. F. Xiao, C. L. Zou, Y. C. Liu, X. F. Jiang, Y. L. Chen, Y. Li, and Q. Gong, Experimental observation of Fano resonance in a single whispering-gallery microresonator, *Appl. Phys. Lett.* **98**, 021116 (2011).
 - [4] Y.-C. Liu, B.-B. Li, and Y.-F. Xiao, Electromagnetically induced transparency in optical microcavities, *Nanophotonics* **6**, 789 (2017).
 - [5] S. Fan, Sharp asymmetric line shapes in side-coupled waveguide-cavity systems, *Appl. Phys. Lett.* **80**, 908 (2002).
 - [6] S. F. Mingaleev, A. E. Miroschnichenko, and Y. S. Kivshar, Coupled-resonator-induced reflection in photonic-crystal waveguide structures, *Opt. Express* **16**, 11647 (2008).
 - [7] L. Y. Mario, S. Darmawan, and M. K. Chin, Asymmetric Fano resonance and bistability for high extinction ratio, large modulation depth, and low power switching, *Opt. Express* **14**, 12770 (2006).
 - [8] Y.-F. Xiao, X.-B. Zou, W. Jiang, Y.-L. Chen, and G.-C. Guo, Analog to multiple electromagnetically induced transparency in all-optical drop-filter systems, *Phys. Rev. A* **75**, 063833 (2007).
 - [9] Z.-H. He, H.-J. Li, S.-P. Zhan, B.-X. Li, Z.-Q. Chen, and H. Xu, Tunable multi-switching in plasmonic waveguide with Kerr nonlinear resonator, *Sci. Rep.* **5**, 15837 (2015).
 - [10] W. Yoshiki, Y. Honda, T. Tetsumoto, K. Furusawa, N. Sekine, and T. Tanabe, All-optical tunable buffering with coupled ultra-high Q whispering gallery mode microcavities, *Sci. Rep.* **7**, 10688 (2017).
 - [11] C. Y. Chao and L. J. Guo, Biochemical sensors based on polymer microrings with sharp asymmetrical resonance, *Appl. Phys. Lett.* **83**, 1527 (2003).
 - [12] X. Zhou, L. Zhang, A. M. Armani, J. Liu, X. Duan, D. Zhang, H. Zhang, and W. Pang, An integrated photonic gas sensor enhanced by optimized Fano effects in coupled microring resonators with an athermal waveguide, *J. Lightwave Technol.* **33**, 4521 (2015).
 - [13] M. Li, X. Wu, L. Liu, X. Fan, and L. Xu, Self-referencing optofluidic ring resonator sensor for highly sensitive biomolecular detection, *Anal. Chem.* **85**, 9328 (2013).
 - [14] Y.-F. Xiao, V. Gaddam, and L. Yang, Coupled optical microcavities: An enhanced refractometric sensing configuration, *Opt. Express* **16**, 12538 (2008).
 - [15] X. Zhou, L. Zhang, A. M. Armani, D. Zhang, X. Duan, J. Liu, H. Zhang, and W. Pang, On-chip biological and chemical sensing with reversed Fano lineshape enabled by embedded microring resonators, *IEEE J. Sel. Top. Quant.* **20**, 5200110 (2014).
 - [16] D. D. Smith, H. Chang, K. Myneni, and A. T. Rosenberger, Fast-light enhancement of an optical cavity by polarization mode coupling, *Phys. Rev. A* **89**, 053804 (2014).
 - [17] G. Guan and F. Vollmer, Polarized transmission spectra of the fiber-microsphere system, *Appl. Phys. Lett.* **86**, 121115 (2005).

- [18] H. Konishi, H. Fujiwara, S. Takeuchi, and K. Sasaki, Polarization-discriminated spectra of a fiber-microsphere system, *Appl. Phys. Lett.* **89**, 121107 (2006).
- [19] P. Bianucci, C. R. Fietz, J. W. Robertson, G. Shvets, and C.-K. Shih, Polarization conversion in a silica microsphere, *Opt. Express* **15**, 7000 (2007).
- [20] P. Bianucci, C. R. Fietz, J. W. Robertson, G. Shvets, and C.-K. Shih, Whispering gallery mode microresonators as polarization converters, *Opt. Lett.* **32**, 2224 (2007).
- [21] M. N. M. Nasir, S. B. Gorajoobi, G. S. Murugan, and M. N. Zervas, Polarization effects in optical microresonators, *J. Opt. Soc. Am. B* **36**, 705 (2019).
- [22] A. T. Rosenberger, E. B. Dale, K. V. Bui, E. K. Gonzales, D. Ganta, L. Ke, and S. R. Rajagopal, Cross-polarization coupling of whispering-gallery modes due to the spin-orbit interaction of light, *Opt. Lett.* **44**, 4163 (2019).
- [23] D. D. Smith, H. Chang, K. A. Fuller, A. T. Rosenberger, and R. W. Boyd, Coupled resonator induced transparency, *Phys. Rev. A* **69**, 063804 (2004).
- [24] A. Naweed, G. Farca, S. I. Shopova, and A. T. Rosenberger, Induced transparency and absorption in coupled whispering-gallery microresonators, *Phys. Rev. A* **71**, 043804 (2005).
- [25] L. Maleki, A. B. Matsko, A. A. Savchenkov, and V. S. Ilchenko, Tunable delay line with interacting whispering-gallery-mode resonators, *Opt. Lett.* **29**, 626 (2004).
- [26] Q. Xu, S. Sandhu, M. L. Povinelli, J. Shakya, S. Fan, and M. Lipson, Experimental Realization of an On-Chip All-Optical Analogue to Electromagnetically Induced Transparency, *Phys. Rev. Lett.* **96**, 123901 (2006).
- [27] X. Yang, M. Yu, D. L. Kwong, and C. W. Wong, All-Optical Analog to Electromagnetically Induced Transparency in Multiple Coupled Photonic Crystal Cavities, *Phys. Rev. Lett.* **102**, 173902 (2009).
- [28] X. Zhou, L. Zhang, W. Pang, H. Zhang, Q. Yang, and D. Zhang, Phase characteristics of an electromagnetically induced transparency analogue in coupled resonant systems, *New J. Phys.* **15**, 103033 (2013).
- [29] C. H. Dong, C.-L. Zou, Y.-F. Xiao, J.-M. Cui, Z.-F. Han, and G.-C. Guo, Modified transmission spectrum induced by two-mode interference in a single silica microsphere, *J. Phys. B: At. Mol. Opt. Phys.* **42**, 215401 (2009).
- [30] Q. Huang, Z. Shu, G. Song, J. Chen, J. Xia, and J. Yu, Electromagnetically induced transparency-like effect in a two-bus waveguides coupled microdisk resonator, *Opt. Express* **22**, 3219 (2014).
- [31] Y. Yang, S. Saurabh, J. Ward, and S. Nic Chormaic, Coupled-mode-induced transparency in aerostatically tuned microbubble whispering-gallery resonators, *Opt. Lett.* **40**, 1834 (2015).
- [32] S. Ramelow, A. Farsi, S. Clemmen, J. S. Levy, A. R. Johnson, Y. Okawachi, M. R. E. Lamont, M. Lipson, and A. L. Gaeta, Strong polarization mode coupling in microresonators, *Opt. Lett.* **39**, 5134 (2014).
- [33] Y. Wang, K. Zhang, S. Zhou, Y.-H. Wu, M.-B. Chi, and P. Hao, Coupled-mode induced transparency in a bottle whispering-gallery-mode resonator, *Opt. Lett.* **41**, 1825 (2016).
- [34] Y. Zheng, J. Yang, Z. Shen, J. Cao, X. Chen, X. Liang, and W. Wan, Optically induced transparency in a micro-cavity, *Light: Sci. Appl.* **5**, e16072 (2016).
- [35] D. V. Strelakov, R. J. Thompson, L. M. Baumgartel, I. S. Grudinin, and N. Yu, Temperature measurement and stabilization in a birefringent whispering gallery mode resonator, *Opt. Express* **19**, 14495 (2011).
- [36] K. Ma, Y. Zhang, H. Su, G. Yi, C. Yu, and J. Wang, Autler-Townes splitting and induced transparency windows in a multi-mode microfiber knot, *Opt. Lett.* **45**, 754 (2020).
- [37] K. Totsuka, N. Kobayashi, and M. Tomita, Slow Light in Coupled-Resonator Induced Transparency, *Phys. Rev. Lett.* **98**, 213904 (2007).
- [38] S. B. Gorajoobi, G. S. Murugan, and M. N. Zervas, Efficient excitation and phase matching of fiber-coupled degenerate whispering gallery modes, *J. Opt. Soc. Am. B* **36**, 2452 (2019).
- [39] M. J. Humphrey, E. Dale, A. T. Rosenberger, and D. K. Bandy, Calculation of optimal fiber radius and whispering-gallery mode spectra for a fiber-coupled microsphere, *Opt. Commun.* **271**, 124 (2007).
- [40] B. Peng, S. K. Ozdemir, W. Chen, F. Nori, and L. Yang, What is and what is not electromagnetically induced transparency in whispering-gallery microcavities, *Nat. Commun.* **5**, 5082 (2014).
- [41] M. Sumetsky, Whispering-gallery-bottle microcavities: The three-dimensional etalon, *Opt. Lett.* **29**, 8 (2004).
- [42] G. S. Murugan, M. N. Petrovich, Y. Jung, J. S. Wilkinson, and M. N. Zervas, Hollow-bottle optical microresonators, *Opt. Express* **19**, 20773 (2011).
- [43] R.-I. Stoian, K. V. Bui, and A. T. Rosenberger, Silica hollow bottle resonators for use as whispering gallery mode based chemical sensors, *J. Opt.* **17**, 125011 (2015).
- [44] R.-I. Stoian, B. K. Lavine, and A. T. Rosenberger, pH sensing using whispering gallery modes of a silica hollow bottle resonator, *Talanta* **194**, 585 (2019).
- [45] V. S. Ilchenko, P. S. Volikov, V. L. Velichansky, F. Treussart, V. Lefèvre-Seguin, J.-M. Raimond, and S. Haroche, Strain-tunable high- Q optical microsphere resonator, *Opt. Commun.* **145**, 86 (1998).
- [46] W. von Klitzing, R. Long, V. S. Ilchenko, J. Hare, and V. Lefèvre-Seguin, Frequency tuning of the whispering gallery modes of silica microspheres for cavity quantum electrodynamics and spectroscopy, *Opt. Lett.* **26**, 166 (2001).
- [47] W. von Klitzing, R. Long, V. S. Ilchenko, J. Hare, and V. Lefèvre-Seguin, Tunable whispering gallery modes for spectroscopy and CQED experiments, *New J. Phys.* **3**, 14 (2001).
- [48] R. Henze, T. Seifert, J. Ward, and O. Benson, Tuning whispering gallery modes using internal aerostatic pressure, *Opt. Lett.* **36**, 4536 (2011).